

Mapping of ESA-CCI land cover data to plant functional types for use in the CLASSIC land model

Libo Wang¹, Vivek K. Arora², Paul Bartlett¹, Ed Chan¹, and Salvatore R. Curasi³⁴

¹Climate Processes Section, Climate Research Division, Environment and Climate Change Canada, Toronto, ON, Canada

²Canadian Centre for Climate Modelling and Analysis, Climate Research Division, Environment and Climate Change Canada, Victoria, BC, Canada

³Department of Geography and Environmental Studies, Carleton University, Ottawa, ON, Canada.

⁴Climate Processes Section, Climate Research Division, Environment and Climate Change Canada, Victoria, BC, Canada.

Corresponding author: Libo Wang, Libo.Wang@ec.gc.ca

Abstract

Plant functional types (PFTs) are used to represent vegetation distribution in land surface models (LSMs). Previous studies have shown large differences in the geographical distribution of PFTs currently used in various LSMs, which may arise from the differences in the underlying land cover products but also the methods used to map or reclassify land cover data to the PFTs that a given LSM represents. There are large uncertainties associated with existing PFT mapping methods since they are largely based on expert judgment and therefore are subjective. In this study, we propose a new approach to inform the mapping or the cross-walking process using analyses from sub-pixel fractional error matrices, which allows for a quantitative assessment of the fractional composition of the land cover categories in a dataset. We use the Climate Change Initiative (CCI) land cover product produced by the European Space Agency (ESA). Previous work has shown that compared to fine-resolution maps over Canada, the ESA-CCI product provides an improved land cover distribution compared to that from the GLC2000 dataset currently used in the CLASSIC (Canadian Land Surface Scheme Including Biogeochemical Cycles) model. A tree cover fraction dataset and a fine-resolution land cover map over Canada are used to compute the sub-pixel fractional composition of the land cover classes in ESA-CCI, which is then used to create a cross-walking table for mapping the ESA-CCI land cover categories to nine PFTs represented in the CLASSIC model. There are large differences between the new PFT distributions and those currently used in the model. Offline simulations performed with the CLASSIC model using the ESA-CCI based PFTs show improved winter albedo compared to that based on the GLC2000 dataset. This emphasizes the importance of accurate representation of vegetation distribution for realistic simulation of surface albedo in LSMs. Results in this study suggest that the sub-pixel fractional composition analyses are an effective

way to reduce uncertainties in the PFT mapping process and therefore, to some extent, objectify the otherwise subjective process.

1. Introduction

Land cover is a critical component of the earth system that affects the exchange of energy, water, and carbon between the land surface and the atmosphere (Pielke et al., 1998; Sterling et al., 2013). Accurate representation of global land cover (LC) is important for land surface models (LSMs) which provide the lower boundary conditions to the atmosphere in numerical weather forecasting, climate, and earth system models (ESMs). Plant functional types (PFTs) are groups of plant species that share similar structural, phenological, and physiological traits, and have been commonly used in LSMs to represent vegetation distribution. This simplification has allowed the simulation of structural attributes of vegetation dynamically within ESMs (Arora & Boer, 2010; Bonan et al., 2003; Krinner et al., 2005). In order to improve the representation of ecosystem ecology and vegetation demographic processes within ESMs, both species-based and trait-based models have been attempted in LSMs (Fisher et al., 2018; Zakharova et al., 2019). However, these individual-based models are computationally too expensive to model biogeochemical processes, especially photosynthesis and the carbon cycle at the global scale (Bonan et al., 2002; Smith et al., 1997; 2001). As a compromise, “cohort-based” models have been developed where individual plants with similar properties (size, age, functional type) are grouped together and have been implemented in some ESMs (Fisher et al., 2018). Though there are limitations in PFTs-based models (Scheiter et al., 2013; Zakharova et al., 2019), PFTs are commonly used in LSMs that participate routinely in the Global Carbon Project (Friedlingstein

et al., 2020) and in ESMs that participate in the Coupled Models Intercomparison Project (CMIP, Wang et al., 2016).

There are three approaches for modeling PFTs: (1) static, where the fractional coverage of PFTs is prescribed and does not vary through time; (2) forced, where the fractional coverage of PFTs is still prescribed but vary through time based on scenarios of land cover/land-use change; and (3) dynamic, where the fractional coverage of PFTs is simulated dynamically with competition for available space and resources between PFTs (Fisher et al., 2018; Melton and Arora, 2016). The number and type of PFTs used in each LSM differ. Global land cover datasets are typically used to derive the fractional coverage of PFTs for use in LSMs. However, large differences exist in both the fractional coverage and the geographical distribution of PFTs, which are caused by differences in the LC datasets themselves but also due to the methods used to map LC datasets to the PFTs represented in various models (Fritz et al, 2011; Hartley et al., 2017; Ottele et al., 2013; Wang et al., 2016).

Since different PFTs are characterized by different physical and biogeochemical processes and parameter values, the spatial distribution and fractional cover of PFTs constitute one of the important geophysical fields that are required for realistic simulation of carbon, water, and energy budgets in LSMs (Arora and Boer, 2010; Betts, 2001). For example, the surface roughness for short or tall vegetation is very different, which affects simulated turbulent exchanges. The surface albedos for needleleaf evergreen trees, broadleaf deciduous trees, and grasslands are also very different, especially during winter when deciduous trees are leafless and short vegetation is largely buried by snow (Bartlett and Versegny, 2015; Moody et al., 2007). Wang et al. (2016) found that the bias in winter albedo in selected boreal forest regions among the CMIP5 models was largely related to biases in leaf area index (LAI) and tree cover fraction.

Model experiments using the MPI-ESM by Georgievski and Hagemann (2019) suggested that uncertainties in vegetation distribution may lead to noticeable variations in near-surface climate variables and large-scale circulation patterns.

The Canadian Land Surface Scheme Including Biogeochemical Cycles (CLASSIC) is an open-source community land model that is designed to address research questions that explore the role of the land surface in the global climate system (Melton et al., 2020). It is the successor to the coupled modelling framework based on the Canadian Land Surface Scheme (CLASS; Verseghy, 1991; 1993) and the Canadian Terrestrial Ecosystem Model (CTEM; Arora and Boer, 2005; Melton and Arora, 2016). The physics and biogeochemistry modules of CLASSIC are based on CLASS and CTEM models, respectively. Since the development of CTEM in the early 2000s, the GLC2000 LC product has been used to specify the spatial distribution of PFTs for CLASSIC when employed as the land surface component of the Canadian Earth system model developed by Environment and Climate Change Canada (Arora et al., 2009; Wang et al., 2006). The Climate Change Initiative (CCI) LC product recently produced by the European Space Agency (ESA) is available at an annual temporal resolution for the period 1992 to 2018 at 300 m spatial resolution (ESA, 2017). It was produced based on broad user consultation, specifically to address the needs of the climate modelling community (Bontemps et al., 2012). Wang et al. (2019) showed that when compared to the finer resolution maps over Canada, the 300 m ESA-CCI product provides much improved LC distribution over Canada compared to that from the 1 km GLC2000 dataset.

To map LC classes to PFTs, a cross-walking table (CW-table) is usually created to assign fractions of each LC class to the different PFTs, such that the sum of the fractions for each class is always one (including fractions of water and bare ground). Previous methods for creating such

CW-tables are mainly based on LC class descriptions, expert knowledge, and the spatial distribution of global biomes (Ottle et al., 2013; Poulter et al., 2011; 2015; Sun and Liang, 2007; Wang et al., 2006). Because LC maps only provide the types of vegetation, and each class can be associated with a broad range of fractional cover of either one or more vegetation types, there are large uncertainties associated with any cross-walking or reclassification process. Wang et al. (2019) reclassified the 10 PFTs in the default CW-table provided in the ESA-CCI LC product user manual (Table 7-2, ESA, 2017) into PFTs represented in the CLASSIC model, and compared them with those based on the GLC2000 dataset. The results suggest that uncertainties in the CW-tables were a major source of large differences in the PFT distributions. In addition, the fractional coverage of tree PFTs based on the default CW-table for the ESA-CCI LC dataset was overestimated along the taiga-tundra transition zone in western Canada, which led to underestimation in winter albedo in CLASSIC offline simulations driven with observation-based reanalysis data (Wang et al., 2018).

The objective of this study is to develop a new CW-table for reclassifying the ESA-CCI LC classes into PFTs represented in the CLASSIC model over the model's Canadian domain, and to compare and assess the performance of CLASSIC offline simulations using the new and existing PFT distributions. Given the close link between the bias in winter albedo and the vegetation distribution in the models (Wang et al., 2016), our assessment of model performance focuses on the simulated surface albedo during the maximum snow accumulation period (February–March for the boreal forest). This simplifies our analyses by excluding the fall/spring transition periods when biases in snow accumulation and melt timing can have a large influence on surface albedo simulated by LSMs (Wang et al., 2014). In addition, we extend the CW-table for the ESA-CCI LC dataset to the global domain. A comprehensive assessment of the impact of the PFT

distribution based on the new CW-table and the ESA-CCI LC dataset on the performance of the CLASSIC model at the global scale is presented in Arora et al. (2022).

2. Data and the CLASSIC model

2.1 The Hybrid LC map over Canada

The United States Geological Survey archive of Landsat imagery has provided open and free access to georeferenced and spectrally corrected analysis-ready imagery (Wulder et al., 2012), which makes it possible to generate time series of LC maps to study LC change. Recently two of these products based on Landsat imagery were generated over Canada, including the North America Land Change Monitoring System (NALCMS) LC dataset (Latifovic et al., 2017) and the Virtual Land Cover Engine (VLCE) framework-generated LC dataset (Hermosilla et al., 2018).

Based on the random forest algorithm and local optimization method, the Canada Centre for Remote Sensing has generated the NALCMS LC maps of Canada for the years 2010 and 2015 at 30 m resolution using Landsat imagery (Latifovic et al., 2017). These LC products are the Canadian contribution to the 30 m resolution 2010/2015 LC map of North America to the joint collaborative effort by the Mexican, American, and Canadian government institutions under the NALCMS umbrella. The NALCMS LC map has 19 classes based on the United Nations Land Cover Classification System (LCCS; Di Gregorio, 2005). Assessment based on reference samples showed an overall accuracy of 76.6% for the year 2010 data (Latifovic et al., 2017), which is used in this study.

VLCE is an automated framework to enable change-informed annual LC mapping using time series of Landsat surface reflectance. Temporally consistent annual LC maps representative of

Canada's forested ecosystems from 1984 to 2012 were generated using the VLCE framework, characterizing LC dynamics following wildfire and harvesting events by Hermosilla et al. (2018). The VLCE maps have 12 LC classes in a hierarchical classification structure following that of the National Forest Inventory. Assessment based on reference samples showed an overall accuracy of 70.3% for the map of the year 2005 (the year with the greatest number of reference samples; Hermosilla et al., 2018). Land cover data from the year 2010 are used in this study. Overall, the 19-class NALCMS product presents a more detailed LC distribution than the 12-class VLCE map over Canada. For example, areas classified as "Exposed/Barren lands" in the VLCE map correspond to either "Sub-polar or polar grassland-lichen-moss", "Sub-polar or polar barren-lichen-moss", or "Barren lands" in the NALCMS map. Areas of cropland are not separated from grassland in the VLCE map. A recent study showed that the wetland class in NALCMS suffers from large uncertainty in forest cover mapping because treed-wetland was not separated from herbaceous wetland in its legend (Wang et al., 2019). To take advantage of both datasets, we created a hybrid product by combining them through the following steps: (1) Reproject the VLCE data from its Lambert Conformal Conic projection to the same Lambert Azimuthal Equal Area projection that is used for the NALCMS data; (2) Replace pixels classified as "Exposed/Barren lands" and "Bryoids" in the VLCE data with the more specific LC classes from the NALCMS data; (3) Replace pixels classified as "Herbs" in the VLCE data with the "Cropland" class in the NALCMS data (remains "Herbs" if not classified as "Cropland" in NALCMS); (4) and merge the rest of LC classes from NALCMS to the corresponding classes in the VLCE data. There are a total of 17 classes in this new hybrid product, which we will henceforth refer to it as the Hybrid LC dataset and is shown in Figure 1.

2.2 The global LC products

The GLC2000 dataset was generated from SPOT/VEG data collected from November 1999 to December 2000 at 1 km resolution (Bartholomé and Belward, 2005). It was produced by 21 separate regional expert groups using an unsupervised image classification method. Based on the LCCS, the regional products were merged into one global product with a generalized LCCS legend of 22 classes. Assessment based on a random sampling of reference sites globally estimated an overall accuracy of 68.6% for the GLC2000 product (Mayaux et al., 2006).

The annual ESA-CCI LC data at 300 m resolution are available for the period 1992-2018, which were generated from baseline data and annual LC changes (ESA, 2017). The baseline data were generated using a combination of machine learning and unsupervised image classification methods from the entire archive of ENVISAT/Medium Resolution Imaging Spectrometer for the period of 2003-2012. The annual LC changes were detected at 1 km resolution from the Advanced Very High Resolution Radiometer time series between 1992 and 1999, SPOT/VEG time series between 1999 and 2013, and the PROBA-V time series between 2013 and 2018. Based on the LCCS legend, the ESA-CCI LC data have 22 level 1 classes, and 15 level 2 sub-classes. Assessment based on the GlobCover validation database estimated an overall accuracy of 71% for the ESA-CCI LC product (ESA, 2017).

2.3 Other datasets

Airborne Lidar has been used to monitor forests since the 1980s and is well suited to estimate vegetation height, volume, and biomass (Hopkinson et al., 2006; Wulder et al., 2008). Vegetation cover percentage for canopy height above 2 m from airborne Lidar data are used to estimate the fraction of tall versus low vegetation for LC classes with a mix of woody and herbaceous vegetation in this study. The Lidar data were collected along 34 survey flights across the boreal

forest of Canada in the summer of 2010 by the Canadian Forest Service (Wulder et al., 2012). A 25 by 25 m tessellation was generated with the approximately 400 m wide Lidar swath, with each cell treated as an individual Lidar plot.

A tree cover fraction (TCF) dataset for 2010 is also used in this study (Hansen et al., 2013; hereafter the Hansen TCF dataset). It was based on Landsat images at 30 m resolution. In contrast to the discrete LC classification datasets (providing a certain number of LC classes) as described above, the Hansen dataset is a vegetation continuous field product (providing tree cover fractions from 0 – 100%), in which the satellite spectral information was used to estimate the TCF in each pixel using a regression tree algorithm (Hansen et al., 2002; 2010). This may better represent heterogeneous areas than is possible by discrete LC classification. Tree cover is defined to exist over pixels where canopy closure is observed for vegetation taller than 5 m in height. Forests are generally defined as woody vegetation taller than 3 m in the regional and global LC datasets. The different definitions of tree heights should not result in much difference in areas with mature forests, such as most boreal forests in Canada.

Simulated surface albedo by the CLASSIC model in offline experiments is evaluated against the Moderate Resolution Imaging Spectroradiometer (MODIS) (MCD43C3) broadband (0.3–5.0 μm) white-sky albedo (Schaaf et al., 2002), with quality flags of 0–2 (75% or more full inversions and 25% or fewer fill values) and solar zenith angles less than 70°. The MODIS albedo product used in this study is at 0.05 degree resolution, and is regridded to the 0.22 degree resolution used for the CLASSIC simulations (see Section 2.4.2).

2.4 The CLASSIC model and simulation setup

2.4.1 The CLASSIC model

204 CLASSIC is the successor to the coupled modelling framework based on the Canadian Land
205 Surface Scheme (CLASS; Verseghy, 1991; 1993) and the Canadian Terrestrial Ecosystem Model
206 (CTEM; Arora and Boer, 2005; Melton and Arora, 2016). The physics and biogeochemistry
207 components of CLASSIC are based on CLASS and CTEM, respectively.

208 For the physics component, the default model's vegetation is represented in terms of the
209 fractional coverage of the four PFTs (needleleaf trees, broadleaf trees, crops, and grasses). The
210 physics component represents a single snow layer with variable depth and a single vegetation
211 canopy layer. As a first-order treatment of subgrid-scale heterogeneity, each grid cell is divided
212 up into four sub-areas, consisting of vegetated and bare soil areas, each with and without snow
213 cover. The visible and near-infrared albedos of each PFT/vegetation category are specified.

214 These albedos are further modified by taking into account the fraction of the ground that is seen
215 from the sky above referred to as the sky view factor (which is modelled as a function of the leaf
216 area index). The albedo of the ground that is seen from the sky above depends on if the ground is
217 snow covered or not but also on the soil moisture of the top soil layer, since wet soil is darker
218 than the dry soil. Canopy snow processes such as interception/unloading, sublimation, and melt
219 are all simulated. The aggregated visible and near-infrared albedos for the bulk canopy are
220 incremented using the current values weighted by the fractional coverage of the vegetation
221 categories (Verseghy 1993). More details can be found in Appendix A. The overall surface
222 albedo of a grid cell is computed as a weighted mean using the fractional coverages for the four
223 sub-areas. Twenty ground layers represent the soil profile, starting with 10 layers of 0.1 m
224 thickness. The thicknesses of the layers gradually increase to 30 m for a total ground depth of
225 over 61 m. Liquid and frozen soil moisture contents, and soil temperature, are determined
226 prognostically for permeable soil layers.

The biogeochemistry component of CLASSIC used here represents vegetation in terms of nine PFTs: Needleleaf Evergreen trees (NLE), Needleleaf Deciduous trees (NLD), Broadleaf Evergreen trees (BLE), Broadleaf Cold Deciduous trees (BCD), Broadleaf Dry Deciduous trees (BDD), C₃ and C₄ Crops (C3C/C4C), and C₃ and C₄ Grasses (C3G/C4G). These nine PFTs map directly onto the four PFTs used by CLASSIC's physics component. When the physics and biogeochemistry components are coupled together, as in the case of simulations carried out in this study, the structural attributes of vegetation including leaf area index, canopy mass, rooting depth, and vegetation height are simulated dynamically as a function of environmental conditions by the biogeochemistry component. When the biogeochemistry component is turned off, specified structural attributes of vegetation for use by the physics component are extracted from look-up tables.

2.4.2 Simulation set up

Gridded meteorological data based on the Climatic Research Unit (CRU, <https://crudata.uea.ac.uk/cru/data/hrg/>) and Japanese reanalysis (JRA) (CRUJRA) are used to drive CLASSIC simulations. The data are constructed by regridding data from the JRA and adjusting where possible to align with the CRU TS 4.05 data. The blended product from January, 1901 to December, 2020 has the 6-hourly temporal resolution of the reanalysis product but monthly means adjusted to match the CRU data (Harris, 2020). The 6-hourly data are disaggregated on-the-fly within CLASSIC into half-hourly data following the methodology by Melton and Arora (2016) for the following seven meteorological variables that are used to force the model: 2 m air temperature, total precipitation, specific humidity, downward solar radiation flux, downward longwave radiation flux, surface pressure, and wind speed. Surface temperature, surface pressure, specific humidity, and wind speed are linearly interpolated. Long-wave

radiation is uniformly distributed across a 6-hour period, and shortwave radiation is diurnally distributed over a day based on a grid cell's latitude and day of year with the maximum value occurring at solar noon. Precipitation is treated following Arora (1997), where the total 6-hour precipitation amount is used to determine the number of wet half hours in a 6-hour period. The 6-hour precipitation amount is then spread randomly, but conservatively, over the wet half-hourly periods. In CLASSIC, the phase of precipitation is determined by a threshold surface air temperature with three options available (Bartlett et al., 2006). The 0°C air temperature threshold is used to partition precipitation into rain or snow in this study. This choice does not have a significant impact on the simulated surface albedo in CLASSIC especially during the February-March months when the snow cover is near its maximum (Wang et al. 2014).

Two simulations over the 1850-2020 historical period are performed using PFTs derived from the ESA-CCI and the GLC2000 datasets respectively, which is the only difference between the two simulations. Static PFTs are used in the simulations where the fractional coverage of PFTs is prescribed and does not vary through time. Besides land cover and meteorological forcings, CLASSIC requires globally averaged atmospheric CO₂ concentration, and geographically varying time-invariant soil texture and soil permeable depth. The atmospheric CO₂ concentration values are provided by the Global Carbon Project protocol (<https://www.globalcarbonproject.org/index.htm>). The soil texture information consists of the percentage of sand, clay, and organic matter and is derived from the SoilGrids250m dataset (Hengl et al., 2017), and permeable soil depth is based on Shangguan et al. (2017). The simulations are performed at a 0.22 degree rotated latitude-longitude grid over a domain including Canada and part of Alaska (Fig. 3). Pre-industrial simulations that correspond to the year 1850 are required prior to doing the historical simulations so that model's carbon pools,

including leaf biomass which determines leaf area index, are spun up to near equilibrium for each land cover. The pre-industrial simulations use 1901-1920 meteorological data repeatedly with atmospheric CO₂ concentration specified at its 1850 level. Each historical simulation is then initialized from its corresponding pre-industrial simulation after it has reached equilibrium (with carbon fluxes to conditions corresponding to the year 1850). For the period 1851-1900, the CRUJRA meteorological data for the first 20 years (1901-1920) are used repeatedly. For the 1901-2020 period the meteorological data corresponding to each actual year are used. The period from 2001 to 2015 was selected for analyzing the simulated results.

3. PFT mapping methods

The CW-table for the ESA-CCI LC dataset is generated through a multi-step process that combines multiple land cover maps at different spatial and categorical resolutions with ancillary data on tree cover and vegetation height (Fig. 2). This includes the following steps: (1) combining two existing land cover maps (NALCMS and VLCE) to produce a harmonized 30 m land cover (Hybrid) map with improved categorical precision (as described in Section 2.1); (2) creating a CW-table for the Hybrid land cover map through a direct mapping of classes from the Hybrid map onto the CLASSIC PFTs, such that each land cover class corresponds to a particular mix of PFTs as represented in CLASSIC. This step is supported by vegetation height data from an airborne Lidar campaign over parts of Canada; (3) computing the sub-pixel fractional composition for classes in the ESA-CCI land cover map (300 m resolution) based on the 30 m Hybrid land cover dataset and the Hansen tree cover fraction dataset; (4) using the sub-pixel fractional composition analysis to create a CW-table for mapping the ESA-CCI land cover classes onto PFTs as represented in CLASSIC; and (5) since the ESA-CCI dataset is global, the CW-table developed over Canada is extended to the whole globe.

3.1 CW-table for mapping Hybrid LC classes to CLASSIC PFTs

Among the nine CLASSIC PFTs, BLE and BDD forests are not present in Canada. These are primarily tropical PFTs as represented in CLASSIC. NLD accounts for less than 1% of coniferous forests in Canada (Wang et al., 2019). Therefore we do not consider NLD, BLE, and BDD from here on in this study. Considering the fine resolution (30 m) of the Hybrid map, especially relative to the model resolution (~16 km) used in this study, we assign fractions of 1.0 to the two pure forest classes (LC210 and LC220), the cropland (LC15), and the five non-vegetative classes (LC16 to LC32) in its CW-table (Table 1). The mixed-wood category (LC230) is split evenly into NLE and BCD in the table based on the definition in the VLCE legend (Hermosilla et al., 2018; Wulder et al., 2003). Note that in Table 1, broadleaf deciduous trees (BDD and BCD) are considered together and separated later into their cold and drought deciduous versions. Similarly, crops and grasses (C_3 and C_4) are considered together and separated later into their C_3 and C_4 varieties. The reason for this is that the separation of broadleaf trees into their cold and deciduous phenotypes is based on latitude (Wang et al., 2006). The separation of crops and grasses based on their photosynthetic pathway (C_3 or C_4) is done based on the C_4 fraction from Still and Berry (2003), which is available at 1° resolution.

CLASSIC explicitly represents shrub PFTs (Meyer et al., 2021), but this work does not use that model version, and therefore the fraction of tall shrubs is assigned to one of the tree PFTs as was done in creating the CW-table for GLC2000 for use with CLASSIC (Wang et al., 2006). Four (LC2 - Sub-polar taiga needleleaf forest, LC50 - Shrubland, LC80 - Wetland, and LC81 - Wetland-treed) out of the 17 classes in the Hybrid map are characterized by a mosaic of trees, shrubs, and herbaceous vegetation. The vegetation coverage for canopy height above 2 m from Lidar plots is used to inform the partitioning of forest (tall vegetation) to non-forest (low

vegetation) fractions for these mixed classes. We overlay the Lidar plots on the Hybrid land cover map in ArcGIS. Samples (20 to 40, note that these classes do not cover large areas in Canada) for the four mixed classes in the Hybrid map are selected where there are Lidar data. The vegetation coverage data (for canopy height above 2 m) from Lidar plots for samples of each class are used to compute an average coverage of tall vegetation (> 2 m) for that class, which is then used to assign forest fractions for these four classes in Table 1.

The distribution of tree species from Beaudoin et al. (2014) is used to guide the separation of coniferous versus broadleaf forest fractions. For example, for the Wetland-treed category (LC81), maps of tree species show that coniferous forests dominate wetland-treed regions, while broadleaf forests are generally non-existent. We, therefore, assign most of the forest fraction to NLE (0.55), only 0.05 to BCD, 0.35 to grasses, and the remaining to the bare ground for LC81 (Table 1). The presence of evergreen shrubs is rare in Canada according to National Forest Inventory ground plots data (Gillis et al., 2005), thus we only assign an estimated tall shrub fraction (0.20) in the shrub class (LC50) to BCD. The sub-polar or polar classes (LC11 to LC13) are located above the treeline and mainly consist of low shrubs and grass. The fractions of grass (including low shrubs) and bare ground are based on field surveys of fractional vegetation cover and tundra PFT data in Bjorkman et al. (2018) and Macander et al. (2020) (by computing the average fractions at the field sites which overlap with the sub-polar or polar classes in the Hybrid/NALCMS land cover map). High-resolution images from Google Earth engine or Bing Maps are also used to examine the ratio of vegetated versus bare ground for all classes in which bare ground is present.

3.2. CW-table for mapping ESA-CCI LC classes to CLASSIC PFTs over Canada

3.2.1 The error and sub-pixel fractional error matrices

A standard approach for the accuracy assessment of LC products is to use an error matrix. It is a square array or table of numbers arranged in rows and columns, in which the classification from the LC product (usually represented by the rows) is compared to the reference data (usually represented by the columns) for each category (Congalton, 1991). The major diagonal of the matrix presents the number of correct classifications indicating the agreement between the LC and the reference data for each category. In practice, fine-resolution regional maps are often used to assess large-scale LC products derived from coarse-resolution data (Cihlar et al., 2003). In such cases, the fine-resolution reference data are aggregated/regridded to match the grid of the coarse-resolution data. Several classes in the reference data may be present in a single coarse-resolution pixel depending on the homogeneity of the landscape. In order to compare the reference and the LC data on a one-to-one basis, the dominant LC class (the class with the most abundant fractions based on all fine-resolution pixels in the reference data) is often assigned to the regridded reference pixel.

The sub-pixel fractional error matrices have been introduced as a more appropriate way of assessing the accuracy of mixed pixels by Latifovic and Olthof (2004). In contrast with an error matrix where only the dominant LC class is used as described above, the sub-pixel fractional error matrix is produced by assigning sub-dominant LC classes from all fine-resolution pixels in the reference data to the corresponding single coarse-resolution pixel. It thus allows a quantitative assessment of the fractional composition of the LC classes in the coarse resolution dataset. In this study, both the 30 m Hansen TCF data and the 30 m Hybrid LC map are used to compute the sub-pixel fractional error matrices of the 300 m ESA-CCI dataset (Table 2 and Table 3). However, the objective here is not an accuracy assessment as in Latifovic and Olthof

(2004) but rather to obtain the fractional composition of the LC classes in the ESA-CCI product and to inform the PFT mapping process. We refer to this process as the sub-pixel fractional composition analyses in the rest of this paper. Sub-pixel fractional composition analyses is first performed for each ecozone and then weighted mean fractions for each ESA-CCI class are computed based on pixel counts in each of the ecozones (see the location of ecozones in Fig. 1). For the Hansen TCF data, results are shown only for the ESA-CCI LC classes containing forests in Canada (Table 2). In the ESA-CCI legend (Table 4), two sub-classes for broadleaf (LC61 and LC62) and needleleaf (LC71 and LC72) forests are included as the closed (>40% forest cover) and open (10-40% forest cover) categories apart from the main classes (LC60 and LC70, closed to open (>15%)). As expected, the TCF is larger for the closed classes than for the main and the open classes (Table 2). In Table 2, we also include ratios of TCF between the main class and the closed class, and between the open class and the closed class. We note that the ratios are different for broadleaf (main class vs. closed class: $68.5/86.7=0.8$; open class vs. closed class: $0.43/86.7=0.43$) and needleleaf (main class vs. closed class: $39.3/61.7=0.6$; open class vs. closed class: $23.2/61.7=0.38$) forests, which need to be taken into account when creating the CW-table for the ESA-CCI dataset.

To obtain representative class compositions of the ESA-CCI dataset, only homogenous ESA-CCI pixels are included in the sub-pixel composition analyses based on the Hybrid LC data. The homogenous pixels are defined following the method in Herold et al. (2008). To quantify landscape heterogeneity, 3×3 pixel neighborhoods are assessed for the ESA-CCI data. A neighborhood is considered homogenous if only one LC class is present. The weighted mean fraction for each class is computed from ecozones with more than 10 homogenous ESA-CCI

pixels for that class (Table 3). Only 13 out of the 37 ESA-CCI classes are included in Table 3, the rest of the classes either have limited presence in Canada or are non-vegetative (Table 4).

In the Hybrid CW-table (Table 1), four LC classes (2, 81, 210, and 230) contribute to the fractional cover of NLE, and five LC classes (50, 80, 81, 220, and 230) contribute to the fractional cover of BCD. In Table 3, we also include an integrated fractional cover (F) for NLE and BCD (last two rows) for each of the ESA-CCI classes based on the following formula:

$$F = \sum_{i=1}^N F1_i * F2_i \quad (1)$$

Where $F1_i$ are fractions in Table 3, $F2_i$ are fractions in Table 1, and N is the number of Hybrid LC classes contributing to NLE (N = 4) or BCD (N = 5) as shown in Table 1. As an example, the fraction of NLE for the LC70 (Tree cover needleleaf evergreen closed to open) in ESA-CCI data in Table 3 (see the NLE row and the column for class 70) is obtained as follows: $F = 0.02 \times 0.20 + 0.17 \times 0.55 + 0.29 \times 1.0 + 0.09 \times 0.5 = 0.44$. This process reduces the subjectivity in assigning the ESA-CCI land cover classes to CLASSIC's two tree PFTs (NLE and BCD) that are present in Canada since the process is based on the high-resolution Hybrid LC data.

3.2.2 CW-table for the ESA-CCI LC dataset over Canada

Table 2 and Table 3 thus form the basis for creating the CW-table for mapping the ESA-CCI LC classes to CLASSIC's PFTs (Fig. 2 and Table 4). For the ESA-CCI class LC61 (Tree cover broadleaved deciduous closed) (not included in Table 3 due to limited presence in Canada), ratios of TCF for LC60 vs LC61 in Table 2 and the fractions of LC60 (Tree cover broadleaved deciduous closed to open) in Table 3 are used to derive fractions for LC61 in Table 4. The remapping of LC62 (Tree cover broadleaved deciduous open) and LC72 (Tree cover needleleaf evergreen open) into CLASSIC's PFTs is done in a similar way. Since NLD is not included in

408 either Table 2 or Table 3, the needleleaf deciduous tree cover classes (LC80-82) are assigned to
409 the same fractions as the needleleaf evergreen tree cover classes (LC70-72). For simplicity, the
410 fractions in Table 3 are rounded to values with either “0” or “5” at the hundredth place when
411 used in Table 4. For the rest of the classes not included in either Table 2 or Table 3, values are
412 based on the default CW-table from the ESA-CCI user guide (Table 7-2, ESA, 2017). The spatial
413 distribution of LC classes is also taken into consideration when determining the fractions in the
414 CW-table. For example, the sparse vegetation class (LC150) is mainly distributed above the
415 treeline in alpine and Arctic tundra environments, thus we only assign 0.05 to BCD, the rest to
416 C3G/C4G and bare ground (Table 4).

417 The six CLASSIC PFTs (those present in Canada) are produced from the Hybrid and the ESA-
418 CCI maps based on Table 1 and Table 4 respectively. The PFTs from the Hybrid map are used as
419 a reference here to map ESA-CCI land cover classes to CLASSIC’s PFTs. To make the spatial
420 distribution of PFTs from ESA-CCI agree better with those from the Hybrid dataset, fractions for
421 the following classes in Table 4 are adjusted upward by 0.05: LC60 from 0.65 to 0.70 for BCD;
422 LC71 and LC81 from 0.80 to 0.85 for NLE; and LC120 from 0.10 to 0.15 for BCD. Values for
423 LC10-20 are also slightly adjusted to reduce crop fractions.

424 Based on Table 4, the fractional coverage of nine CLASSIC PFTs are also produced on a global
425 scale and used in offline CLASSIC simulations in Arora et al. (2022), who carry out a
426 comprehensive assessment of the impact of using two different LC datasets (ESA-CCI versus
427 GLC2000) for representing the nine PFTs in the CLASSIC model. However, some adjustments
428 to Table 4 are found to be necessary. This is because fractions of NLE (Needleleaf evergreen
429 forests) in Eurasia are found to be too low relative to the Hansen TCF data, with maximum
430 values only around 0.45 in most NLE dominated areas, where the maximum TCF from the

Hansen dataset is around 0.80. This indicates that the needleleaf evergreen forests classes (LC 70-72) in the ESA-CCI map may represent different forest/tree cover fractions in Canada and Eurasia, which is confirmed by sub-pixel fractional composition analyses based on the Hansen TCF dataset. Details are presented in Appendix B.

4. Results

4.1 Comparison of PFTs from Hybrid, ESA-CCI, and GLC2000 data

Figure 3 shows the spatial distribution of PFTs derived from the Hybrid, ESA-CCI, and GLC2000 LC datasets respectively. C₄ crops (C₄C) and grasses (C₄G) are sparse in Canada as would be expected since C₄ PFTs grow only in warmer temperatures when the average monthly temperature exceeds 22 °C (Fox et al., 2018). Based on the fractional distribution of C₄ vegetation in Still and Berry (2003) and the Hybrid map, the average fraction is 0.5% for C₄ crops and 0.1% for C₄ grasses in Canada. Therefore, only four out of the six PFTs (those present in Canada) are shown in Figure 3. In general, the spatial distributions of the PFTs from the ESA-CCI and the Hybrid datasets agree well except for C₃ grasses (C₃G) (Fig. 3j and Fig. 3k). This is not surprising given that the CW-table for the ESA-CCI dataset is based on the Hybrid map. Areas mapped as C₃G in Hybrid (Fig. 3j), were mainly classified as sparse vegetation (LC150) in the ESA-CCI legend (Table 4). However, LC150 from ESA-CCI was also found in some areas of the high Arctic islands, where barren land is the dominant class in the Hybrid map (grey coloured areas in Fig. 1). If too much grass were assigned to LC150, it would yield unrealistically large fractional coverage of grass in the high Arctic islands. In Table 4, for LC150, 0.05 is assigned to BCD, 0.35 to grasses, and the rest to the bare ground for LC150, which yields a total vegetation cover of 40% and is more than the definition (<15% vegetation)

used in the ESA-CCI legend. Yet, this still results in less C3G and less bare ground in the ESA-CCI map (Fig. 3k and Fig. 3n) than those from the Hybrid map (Fig. 3j and Fig. 3m). This suggests that it is not ideal to classify areas in the high Arctic islands and in the Arctic tundra region as being in the same land cover category.

There are large differences in the spatial distribution of the PFTs based on the GLC2000 LC product and those based on the Hybrid and ESA-CCI datasets (Fig. 3 and Fig. 4). Relative to PFTs from ESA-CCI, GLC2000 has less NLE and more BCD in northwestern Canada, and more NLE in southern and eastern Canada (Fig. 4a and Fig. 4b). GLC2000 based CLASSIC PFT fractions also exhibit more crops, less grass, and more bare ground (Fig. 4c-4e). These differences partly stem from the differences in the ESA-CCI and GLC2000 LC datasets, but are also due to the fact how the fractions in the CW-tables of the two datasets are used to translate LC data to fractional coverage of PFTs as demonstrated in Wang et al. (2019).

4.2 Bias in simulated surface albedo and LAI

The top row of Figure 5 shows the bias in winter albedo (March) simulated by CLASSIC when using PFT distributions based on the ESA-CCI (Fig. 5a) and GLC2000 products (Fig. 5b). While model biases are the result of both the driving geophysical and meteorological data that are used to force the model, as well as the model itself, the comparison between the two simulations does show the effect of differences in the distribution of PFTs. Relative to observed surface albedo from MODIS, there are relatively large negative biases in the southwest of Hudson Bay and central Quebec, while there are relatively large positive biases in western Canada and Alaska in the simulation when using the GLC2000 product to obtain PFT distributions (Fig. 5b). Both the negative and the positive biases are largely reduced in the simulation using PFT distributions

based on the ESA-CCI product (Fig. 5a). The lower row of Figure 5 shows the spatial distribution of the difference in surface albedo (Fig. 5c) and leaf area index (Fig. 5d) between the two simulations, which are closely correlated ($r = -0.85$). Given the same meteorological forcing dataset is used to drive both simulations, the differences in the simulated LAI are due mainly to the different PFT distributions used in the two simulations. Since NLE is the only PFT with $LAI > 0$ during winter in Canada, the LAI difference in March as shown in Figure 5d is mainly due to the different fractional coverage of NLE based on the ESA-CCI and GLC2000 products (Fig. 4a).

In contrast, the large positive albedo biases (up to ~ 0.4) in southern Canada are more or less the same in both simulations (Fig. 5a and Fig. 5b), where the dominant PFT is C3 crops (Fig. 3h and Fig. 3i). Those positive albedo biases are likely due to the standing crop stubble and the lack of the representation of blowing snow and its sublimation currently in CLASSIC (Harder et al., 2018; Pomeroy et al., 1993). Harder et al. (2018) showed that the height of the stubble over wheat and canola field in Saskatchewan, Canada may range from 10 to 40 cm, with a maximum PAI (plant area index) of 1.0. Wang et al. (2016) showed that surface albedo in CLASSIC decreased exponentially with increasing PAI for the bare or snow-covered canopy over snow, while most reductions of the albedo were achieved through the increase of PAI from 0 to 1.0. They showed that surface albedo decreased from 0.75 to 0.31 in CLASSIC when PAI increased from 0 to 1.0 for the bare canopy over snow, which appears to account for most of the positive albedo biases in the agricultural areas of southern Canada (Fig. 5a and Fig. 5b). Improvements to the crop module of CLASSIC to improve cropland albedo are currently being considered.

5. Summary and conclusions

497 A hybrid land cover map at 30 m resolution is created by merging the NALCMS and VLCE land
498 cover products over Canada. Vegetation height data from Lidar plots, tree species, and high
499 resolution images are used to inform the creation of a CW-table for mapping the 17 LC classes
500 of the Hybrid map to six CLASSIC PFTs that are present in Canada. Both the Hybrid map and
501 the Hansen tree cover fraction data are used to compute the sub-pixel fractional composition of
502 the LC classes in the ESA-CCI LC dataset, which is then used to create a cross-walking table for
503 mapping the 37 ESA-CCI categories to CLASSIC PFTs over the model's Canadian domain.
504 Based on the new CW-tables, PFT distributions are produced from the Hybrid and the ESA-CCI
505 LC products, respectively, and are compared with those based on the GLC2000 dataset currently
506 used in CLASSIC. The results show that the spatial distribution of PFTs from the ESA-CCI
507 dataset is in better agreement with those from the Hybrid map, while there are large differences
508 in the PFTs from the GLC2000 dataset and from the Hybrid/ESA-CCI datasets. The CW-table
509 developed over Canada is adjusted and also used to map PFTs based on the ESA-CCI LC
510 product for use in CLASSIC simulations at the global scale.

511 Our PFT mapping approach for the ESA-CCI dataset is mainly based on sub-pixel fractional
512 composition analyses using the Hybrid map and the Hansen tree cover fraction data, and
513 therefore the accuracy of the latter two datasets affects the PFT mapping process. Some LC
514 categories in the ESA-CCI legend either have limited presence or no presence in Canada, such as
515 the Needleleaf deciduous trees, Broadleaf Evergreen trees, and Broadleaf Dry Deciduous trees
516 etc., and the sub-pixel fractional composition analyses therefore can not be performed for these
517 LC categories. The needleleaf deciduous tree cover classes are assigned to the same fractions as
518 the needleleaf evergreen tree cover classes in the CW-table, and values based on the default CW-
519 table from the ESA-CCI user guide are used for the other LC categories. Therefore potentially

large uncertainties may be associated with these classes in the resulting fractional coverage of PFTs especially at the global scale. Similar analyses for other regions (e.g. Eurasia and tropics) for which high quality regional land cover maps are available will be helpful in reducing these uncertainties in the future work. In addition, the exercise of mapping PFTs at the global scale in this study reveals that there are inconsistencies in the representation of fractional coverage for some LC categories in the ESA-CCI map for different regions of the globe. Future improvements in the consistency of the LC categories globally in the ESA-CCI LC product would greatly benefit the land surface and the earth system modelling community. In the meantime, caution should be exercised when using this product for mapping PFTs represented in any LSM based on a single cross-walking table at the global scale.

CLASSIC simulations driven with meteorological data from the CRU-JRA product show that the simulated winter albedo is improved when using PFT distributions based on the ESA-CCI LC product compared to that based on the GLC2000 product, which is consistent with findings from previous studies. While, CLASSIC simulations could also have been performed using its PFT distributions based on the Hybrid LC product, the reason for using the ESA-CCI based PFT fractions for CLASSIC is that ESA-CCI is a global product. CLASSIC simulations are routinely performed at the global scale both in the framework of the Canadian Earth System Model (Swart et al., 2019), where CLASSIC serves as its land component, and offline where global CLASSIC simulations driven with the CRU-JRA meteorological data contribute to the annual global carbon budget assessments of the Global Carbon Project (Friedlingstein et al., 2020; Seiler et al., 2021). Untreated crop stubble appears to be contributing to the positive winter albedo biases in southern Canada, which needs to be addressed in a future version of CLASSIC. These results underscore

the importance of accurate representation of vegetation distribution in a realistic simulation of surface albedo in LSMs.

Previous methods for mapping PFTs from LC datasets have mainly been based on class descriptions, expert knowledge, and the spatial distribution of global biomes, which is a largely subjective process. As a consequence, a PFT method developed for mapping one LC dataset to PFTs represented in one model can not be easily transferred to other LC datasets even for deriving PFTs in the same model. The development of satellite and computing technology has enabled the creation of more detailed global LC products at finer spatial resolutions in recent years, however, the lack of an objective PFT mapping method impedes the implementation of the new improved LC products in LSMs. Here, we have proposed a method to inform the cross-walking process using sub-pixel fractional composition analyses based on a tree cover fraction dataset and a fine-resolution LC map. Our results suggest that the sub-pixel fractional composition analyses provide an effective way to reduce uncertainties in the cross-walking process and therefore, to some extent, objectifies the otherwise subjective process. The PFT mapping approach developed in this study can also be applied to other LC datasets for mapping PFTs used in other LSMs.

Appendix A

In CLASSIC, the surface albedo for a canopy over snow (α) is:

$$\alpha = \alpha_c(1 - \chi)(1 - f_{snow}) + \alpha_{c,snow}(1 - \chi)f_{snow} + \alpha_{snow}\chi\tau_c \quad (1)$$

$$\chi = \exp(-K*PAI) \quad (2)$$

calculated using separate parameters (α_c , $\alpha_{c,snow}$, τ_c and K) for both the visible (VIS) and near infrared (NIR) bands, where α_c is the snow-free canopy albedo, $\alpha_{c,snow}$ the snow-covered canopy albedo, f_{snow} the fraction of the canopy with snow on it, α_{snow} the snowpack albedo. τ_c is canopy transmissivity and is modeled using a Beer's law approach, ignoring multiple reflections (Verseghy *et al.* 1993). K is an extinction coefficient that varies with vegetation type. The appearance of τ_c in the last term of Eq.1 accounts for the shading of the snowpack by the canopy, converting the simulated snowpack albedo to an effective value of the canopy gaps. PAI is plant area index which is the sum of leaf area index and stem area index.

Appendix B

Based on Table 4, the fractional coverage of nine CLASSIC PFTs are also produced on a global scale. However, some adjustments to Table 4 were found necessary. This is because fractions of NLE (Needleleaf evergreen forests) in Eurasia are found to be too low relative to the Hansen TCF data, with maximum values of only around 0.45 in most NLE dominated areas, where the maximum TCF from the Hansen dataset is around 0.80. Needleleaf evergreen forests are represented by LC classes 70 (closed to open), 71 (closed), and 72 (open). Examining the ESA-CCI LC map shows that in Eurasia nearly all needleleaf evergreen forests are classified as LC70 (closed to open), with only less than 400 pixels as LC71 (closed), and none as LC72 (open). In contrast, in Canada 36% of needleleaf evergreen forest are classified as LC70 (closed to open), 64% as LC71 (closed), and less than 1% as LC72 (open). This is understandable given that sub-pixel classes were only assigned where surface samples were available (ESA, 2017). Sub-pixel fractional composition analyses of the ESA-CCI classes based on the Hansen TCF dataset show

that in Eurasia TCF for LC70 (closed to open) is 66% and for LC71 (closed) is 35% (note the few pixels within this class). This is in contrast with those in Canada where the TCF for LC70 (closed to open) is 39% and for LC71 (closed) is 62%, explaining the too low NLE fractions in Eurasia when mapping PFTs based on Table 4, and also the too high TCF in northwestern Canada when mapping PFTs based on the default CW-table (Wang et al., 2018). In order to apply Table 4 globally, the original LC70 (closed to open) was split into two classes: LC73 (a new class) which is the same as LC70 over Canada (and zero everywhere else), and LC70 (revised) which is the same as before except zero over Canada. The fractions for the new LC70 class are made the same as for LC71 in Table 4, which applies to NLE outside of Canada. Essentially, the closed-to-open needleleaf forest LC70 class over Eurasia is treated as the closed needleleaf forest.

Acknowledgements.

We'd like to thank Mike Brady (ECCC) for his help with data processing and especially for creating the Hybrid map, and Mike Wulder from the Canadian Forest Service of Natural Resources Canada for providing the Lidar plots data and for helping interpret the Lidar data and the VLCE land cover map.

References

605 Arora, V.: Land surface modelling in general circulation models: a hydrological perspective,
 606 PhD thesis, Department of Civil and Environmental Engineering, University of Melbourne,
 607 1997.

608 Arora, V. K., Boer, G. J.: A parameterization of leaf phenology for the terrestrial ecosystem
 609 component of climate models. *Glob. Chang. Biol.*, 11, 39–59, 2005.

610 Arora, V. K. and Boer, G. J.: Uncertainties in the 20th century carbon budget associated with
 611 land use change, *Glob. Change Biol.*, 16, 3327–3348, [https://doi.org/10.1111/j.1365-](https://doi.org/10.1111/j.1365-2486.2010.02202.x)
 612 [2486.2010.02202.x](https://doi.org/10.1111/j.1365-2486.2010.02202.x), 2010.

613 Arora, V. K., Boer, G. J., Christian, J. R., Curry, C. L., Denman, K. L., Zahariev, K., Flato, G.
 614 M., Scinocca, J. F., Merryfield, W. J., and Lee, W. G.: The Effect of Terrestrial Photosynthesis
 615 Down Regulation on the Twentieth-Century Carbon Budget Simulated with the CCCma Earth
 616 System Model, *J. Clim.*, 22, 6066–6088, <https://doi.org/10.1175/2009JCLI3037.1>, 2009.

617 Arora, V. K., Seiler, C., Wang, L., and Kou-Giesbrecht, S.: Towards an ensemble-based
 618 evaluation of land surface models in light of uncertain forcings and observations, *EGUsphere*
 619 [preprint], <https://doi.org/10.5194/egusphere-2022-641>, 2022.

620 Beaudoin, A., Bernier, P.Y., Guindon, L., Villemaire, P., Guo, X.J., Stinson, G., Bergeron, T.,
 621 Magnussen, S., and Hall, R.J.: Mapping attributes of Canada’s forests at moderate resolution
 622 through kNN and MODIS imagery, *Can. J. For. Res.* 44: 521–532, [dx.doi.org/10.1139/cjfr-2013-](https://doi.org/10.1139/cjfr-2013-0401)
 623 [0401](https://doi.org/10.1139/cjfr-2013-0401), 2014.

624 Bartholomé, E., and Belward, A. S.: GLC2000: A new approach to global land cover mapping
 625 from Earth Observation data, *Int. J. Remote Sens.*, 26, 1959–1977, 2005.

626 Bartlett, P. A., MacKay, M. D., and Verseghy, D. L.: Modified snow algorithms in the Canadian
 627 land surface scheme: Model runs and sensitivity analysis at three boreal forest stands, *Atmos.–*
 628 *Ocean*, 44, 207–222, 2006.

629 Bartlett, P. A., and Verseghy, D. L.: Modified treatment of intercepted snow improves the
 630 simulated forest albedo in the Canadian land surface scheme, *Hydrol. Process.*, 29, 3208–3226,
 631 <https://doi.org/10.1002/hyp.10431>, 2015.

632 Betts, R. A.: Biogeophysical impacts of land use on present-day climate: near-surface
 633 temperature change and radiative forcing, *Atmos. Sci. Lett.*, 2, 39–51,
 634 <https://doi.org/10.1006/asle.2001.0037>, 2001.

635 Bjorkman, A. D., Myers-Smith, I. H., Elmendorf, S.C. et al.: Plant functional trait change across
 636 a warming tundra biome, *Nature*, 562, 57–62, <https://doi.org/10.1038/s41586-018-0563-7>, 2018.

637 Bonan, G. B., Levis, S., Kergoat, L., Oleson, K. W.: Landscapes as patches of plant functional
 638 types: An integrating concept for climate and ecosystem models, *Global Biogeochem. Cycles*,
 639 16(2), 1021, <https://doi.org/10.1029/2000GB001360>, 2002.

640 Bonan, G. B., Levis, S., Sitch, S., Vertenstein, M., and Oleson, K. W.: A dynamic global
 641 vegetation model for use with climate models: Concepts and description of simulated vegetation
 642 dynamics. *Global Change Biology*, 9, 1543–1566, 2003.

643 Bontemps, S., Herold, M., Kooistra, L., van Groenestijn, A., Hartley, A., Arino, O., Moreau, I.,
 644 Defourny, P.: Revisiting land cover observation to address the needs of the climate modeling
 645 community, *Biogeosciences*, 9, 2145–2157, <https://doi.org/10.5194/bg-9-2145-2012>, 2012.

646 Di Gregorio, A.: Land Cover Classification System – Classification concepts and user manual
647 for Software version 2, FAO Environment and Natural Resources Service Series, No. 8, Rome,
648 208pp, 2005.

649 ESA: Land Cover CCI Product User Guide Version 2. Tech. Rep., Available at:
650 maps.elie.ucl.ac.be/CCI/viewer/download/ESACCI-LC-Ph2-PUGv2_2.0.pdf, 2017.

651 Fisher, R. A., Koven, C. D., Anderegg, W. R. L. et al.: Vegetation demographics in Earth System
652 Models: A review of progress and priorities. *Glob Change Biol.*, 24, 35–54,
653 <https://doi.org/10.1111/gcb.13910>, 2018.

654 Fox, D.L., Pau, S., Taylor, L., Strömberg, C. A. E., Osborne, C.P., Bradshaw, C., Conn, S.,
655 Beerling, D.J., and Still, C.J.: climatic Controls on C4 Grassland Distributions During the
656 Neogene: A Model-Data Comparison, *Frontiers in Ecology and Evolution*, 6,
657 <https://doi.org/10.3389/fevo.2018.00147>, 2018.

658 Friedlingstein, P., O'Sullivan, M., Jones, M. W., Andrew, R. M., Hauck, J., Olsen, A., Peters, G.
659 P., Peters, W., Pongratz, J., Sitch, S., Le Quéré, C., Canadell, J. G., Ciais, P., Jackson, R. B.,
660 Alin, S., Aragão, L. E. O. C., Arneeth, A., Arora, V., Bates, N. R., Becker, M., Benoit-Cattin, A.,
661 Bittig, H. C., Bopp, L., Bultan, S., Chandra, N., Chevallier, F., Chini, L. P., Evans, W., Florentie,
662 L., Forster, P. M., Gasser, T., Gehlen, M., Gilfillan, D., Gkritzalis, T., Gregor, L., Gruber, N.,
663 Harris, I., Hartung, K., Haverd, V., Houghton, R. A., Ilyina, T., Jain, A. K., Joetzjer, E., Kadono,
664 K., Kato, E., Kitidis, V., Korsbakken, J. I., Landschützer, P., Lefèvre, N., Lenton, A., Lienert, S.,
665 Liu, Z., Lombardozzi, D., Marland, G., Metzl, N., Munro, D. R., Nabel, J. E. M. S., Nakaoka, S.-
666 I., Niwa, Y., O'Brien, K., Ono, T., Palmer, P. I., Pierrot, D., Poulter, B., Resplandy, L.,
667 Robertson, E., Rödenbeck, C., Schwinger, J., Séférian, R., Skjelvan, I., Smith, A. J. P., Sutton,

668 A. J., Tanhua, T., Tans, P. P., Tian, H., Tilbrook, B., van der Werf, G., Vuichard, N., Walker, A.
 669 P., Wanninkhof, R., Watson, A. J., Willis, D., Wiltshire, A. J., Yuan, W., Yue, X., and Zaehle,
 670 S.: Global Carbon Budget 2020, *Earth Syst. Sci. Data*, 12, 3269–3340,
 671 <https://doi.org/10.5194/essd-12-3269-2020>, 2020.

672 Fritz, S., See, L., McCallum, I., Schill, C., Obersteiner, M., van der Velde, M., Boettcher, H.,
 673 Havlík, P., Achard, F.: Highlighting continued uncertainty in global land cover maps for the user
 674 community, *Environ. Res. Lett.*, 6, 44005. <https://dx.doi.org/10.1088/1748-9326/6/4/044005>,
 675 2011.

676 Georgievski, G., Hagemann, S.: Characterizing uncertainties in the ESA-CCI land cover map of
 677 the epoch 2010 and their impacts on MPI-ESM climate simulations, *Theor. Appl. Climatol.*, 137,
 678 1587–1603, <https://doi.org/10.1007/s00704-018-2675-2>, 2019.

679 Gillis, M. D., Omule, A. Y., and Brierley, T.: Monitoring Canada's forests: The National Forest
 680 Inventory, *The Forestry Chronicle*, 81(2): 214–221, <https://doi.org/10.5558/tfc81214-2>, 2005.

681 Harris, I. C.: CRU JRA v2.1: A forcings dataset of gridded land surface blend of Climatic
 682 Research Unit (CRU) and Japanese reanalysis (JRA) data; Jan. 1901 - Dec. 2019, Centre for
 683 Environmental Data Analysis, University of East Anglia Climatic Research Unit,
 684 <https://catalogue.ceda.ac.uk/uuid/10d2c73e5a7d46f4ada08b0a26302ef7>, 2020

685 Hartley, A. J., MacBean, N., Georgievski, G., Bontemps, S.: Uncertainty in plant functional type
 686 distributions and its impact on land surface models, *Remote Sens. Environ.*, 203, 71–89,
 687 <https://doi.org/10.1016/j.rse.2017.07.037>, 2017.

688 Harder, P., Warren D. H., and Pomeroy, J. W.: Modeling the Snowpack Energy Balance during
689 Melt under Exposed Crop Stubble, *J. Hydrometeorol.*, 19, 1191-1214, [https://DOI:](https://doi.org/10.1175/JHM-D-18-0039.1)
690 10.1175/JHM-D-18-0039.1, 2018.

691 Hansen, M. C., DeFries, R. S., Townshend, J. R. G., Sohlberg, R., Dimiceli, C., Carroll, M. L.:
692 Towards an operational MODIS continuous field of percent tree cover algorithm: Examples us-
693 ing AVHRR and MODIS data, *Remote Sens. Environ.*, 83, 303–319, 2002.

694 Hansen, M. C., Stehman, S. V., Potapov, P. V.: Quantification of global gross forest cover loss,
695 *P. Natl. Acad. Sci.*, 107, 8650–8655, <https://doi.org/10.1073/pnas.0912668107>, 2010.

696 Hansen, M. C., Potapov, P. V., Moore, R., Hancher, M., Turubanova, S. A., Tyukavina, A.,
697 Thau, D., Stehman, S. V., Goetz, S. J., Loveland, T.R., et al.: Highresolution global maps of
698 21st-century forest cover change, *Science*, 342, 850–853, [https://DOI: 10.1126/science.1244693](https://doi.org/10.1126/science.1244693),
699 2013.

700 Hengl, T., Mendes de Jesus, J., Heuvelink, G. B. M., Ruiperez Gonzalez, M., Kilibarda, M.,
701 Blagotić, A., Shangguan, W., Wright, M. N., Geng, X., Bauer-Marschallinger, B., Guevara, M.
702 A., Vargas, R., MacMillan, R. A., Batjes, N. H., Leenaars, J. G. B., Ribeiro, E., Wheeler, I.,
703 Mantel, S., and Kempen, B.: SoilGrids250m: Global gridded soil information based on machine
704 learning, *PLOS ONE*, 12, 1–40, <https://doi.org/10.1371/journal.pone.0169748>, 2017

705 Hermosilla, T., Wulder, M. A., White, J. C., Coops, N. C., Hobart, G.W.: Disturbance informed
706 annual land cover classification maps of Canada’s forested ecosystems for a 29-year Landsat
707 time series. *Can. J. Remote. Sens.*, 44, 67–87. <https://doi.org/10.1080/07038992.2018.1437719>,
708 2018.

709 Herold, M., Mayaux, P., Woodcock, C. E., BaESACCini, A., Schmulius, C.: Some Challenges
 710 in Global Land Cover Mapping: An Assessment of Agreement and Accuracy in Existing 1 km
 711 Datasets, *Remote Sens. Environ.*, 112, 2538–2556, 2008.

712 Hopkinson, C., Chasmer, L., Lim, K., Treitz, P., and Creed, I.: Towards a universal lidar canopy
 713 height indicator, *Canadian Journal of Remote Sensing*, 32 (2), 139-152, [https://doi:](https://doi.org/10.5589/m06-006)
 714 10.5589/m06-006, 2006.

715 Krinner, G., Viovy, N., de Noblet-Ducoudre, N., Ogee, J., Polcher, J., Friedlingstein, P. et al.: A
 716 dynamic global vegetation model for studies of the coupled atmosphere-biosphere system,
 717 *Global Biogeochemical Cycles*, 19(1), GB1015, 2005.

718 Latifovic, R., Pouliot, D., and Olthof, I.: Circa 2010 Land Cover of Canada: Local Optimization
 719 Methodology and Product Development, *Remote Sens.*, 9, 1098,
 720 <https://doi.org/10.3390/rs9111098>, 2017.

721 Latifovic, R., and Olthof, I.: Accuracy assessment using sub-pixel fractional error matrices of
 722 global land cover products derived from satellite data, *Remote Sens. Environ.*, 90, 153–165,
 723 2004.

724 Macander, M. J., Frost, G. V., Nelson, P. R., and Swingley, C. S.: ABoVE: Tundra Plant
 725 Functional Type Continuous-Cover, North Slope, Alaska, 2010-2015, ORNL DAAC, Oak
 726 Ridge, Tennessee, USA, <https://doi.org/10.3334/ORNLDAAAC/1830>, 2020.

727 Mayaux, P., Eva, H., Gallego, J., Strahler, A. H., Herold, M., Agrawal, S., Naumov, S., De
 728 Miranda, E. E., Di Bella, C. M., Ordoyne, C., et al.: Validation of the Global Land Cover 2000
 729 Map. *IEEE Trans. Geosci. Remote Sens.*, 44, 1728–1739, 2006.

730 Melton, J. R. and Arora, V. K.: Competition between plant functional types in the Canadian
 731 Terrestrial Ecosystem Model (CTEM) v. 2.0, *Geosci Model Dev*, 9, 323–361,
 732 <https://doi.org/10.5194/gmd-9-323-2016>, 2016.

733 Melton, J. R., Arora, V. K., Wisernig-Cojoc, E., Seiler, C., Fortier, M., Chan, E., and
 734 Teckentrup, L.: CLASSIC v1.0: the open-source community successor to the Canadian Land
 735 Surface Scheme (CLASS) and the Canadian Terrestrial Ecosystem Model (CTEM) – Part 1:
 736 Model framework and site-level performance, *Geosci. Model Dev. Discuss.*, 1–40,
 737 <https://doi.org/10.5194/gmd-2019-329>, 2019.

738 Meyer, G., Humphreys, E. R., Melton, J. R., Cannon, A. J., and Lafleur, P. M.: Simulating
 739 shrubs and their energy and carbon dioxide fluxes in Canada’s Low Arctic with the Canadian
 740 Land Surface Scheme Including biogeochemical Cycles (CLASSIC), *Biogeosciences*, 18, 3263–
 741 3283, 2021.

742 Moody, E. G., King, M. D., Schaaf, C. B., Hall, D. K., Platnick, S.: Northern Hemisphere five-
 743 year average (2000–2004) spectral albedos of surfaces in the presence of snow: statistics
 744 computed from Terra MODIS land products, *Remote Sens. Environ.*, 111, 337–345, [https://DOI:](https://DOI:10.1016/j.rse.2007.03.026)
 745 [10.1016/j.rse.2007.03.026](https://DOI:10.1016/j.rse.2007.03.026), 2007.

746 Ottlé, C., Lescure, J., Maignan, F., Poulter, B., Wang, T., and Delbart, N.: Use of various remote
 747 sensing land cover products for plant functional type mapping over Siberia, *Earth Syst. Sci. Data*,
 748 5, 331–348, <https://doi:10.5194/essd-5-331-2013>, 2013.

749 Pielke, R. A., Avissar, R., Raupach, M., Dolman, A. J., Zeng, X., Denning, S.: Interactions
 750 between the atmosphere and terrestrial ecosystem: influence on weather and climate, *Global*
 751 *Change Biol.*, 4, 461–475, 1998.

752 Poulter, B., Ciais, P., Hodson, E., Lischke, H., Maignan, F., Plummer, S., and Zimmermann, N.
 753 E.: Plant functional type mapping for earth system models, *Geosci. Model Dev.*, 4, 993–1010,
 754 <https://doi.org/10.5194/gmd-4-993-2011>, 2011.

755 Poulter, B., MacBean, N., Hartley, A., Khlystova, I., Arino, O., Betts, R., Bontemps, S.,
 756 Boettcher, M., Brockmann, C., Defourny, P., Hagemann, S., Herold, M., Kirches, G., Lamarche,
 757 C., Lederer, D., Ottlé, C., Peters, M., and Peylin, P.: Plant functional type classification for earth
 758 system models: results from the European Space Agency's Land Cover Climate Change
 759 Initiative, *Geosci. Model Dev.*, 8, 2315–2328, <https://doi.org/10.5194/gmd-8-2315-2015>, 2015.

760 Pomeroy, J. W., Gray, D. m., and Landine, P. G.: The Prairie Blowing Snow Model:
 761 Characteristics, validation, operation. *J. Hydrol.*, 144, 165–192, [https://doi.org/10.1016/0022-](https://doi.org/10.1016/0022-1694(93)90171-5)
 762 [1694\(93\)90171-5](https://doi.org/10.1016/0022-1694(93)90171-5), 1993.

763 Schaaf, C. B., et al.: First operational BRDF, albedo nadir reflectance products from MODIS,
 764 *Remote Sens. Environ.*, 83, 135–148, [https://doi.org/10.1016/S0034-4257\(02\)00091-3](https://doi.org/10.1016/S0034-4257(02)00091-3), 2002.

765 Scheiter, S., Langan, L., Higgins, S.I.: Next-generation dynamic global vegetation models:
 766 learning from community ecology, *New Phytol.*, 198, 957–969,
 767 <https://doi.org/10.1111/nph.12210>, 2013.

768 Seiler, C., Melton, J. R., Arora, V. K., and Wang, L.: CLASSIC v1.0: the open-source
 769 community successor to the Canadian Land Surface Scheme (CLASS) and the Canadian
 770 Terrestrial Ecosystem Model (CTEM) – Part 2: Global Benchmarking, *Geoscientific Model*
 771 *Development*, <https://doi.org/10.5194/gmd-14-2371-2021>, 2021.

772 Shangguan, W., Hengl, T., Mendes de Jesus, J., Yuan, H., and Dai, Y.: Mapping the global depth
 773 to bedrock for land surface modeling, *J. Adv. Model. Earth Syst.*, 9, 65–88,
 774 <https://doi.org/10.1002/2016MS000686>, 2017.

775 Smith, T. M., Shugart, H. H., and Woodward, F. I.: Plant functional types: their relevance to
 776 ecosystem properties and global change, Cambridge University Press, New York, 369 pp., 1997.

777 Smith, B., Prentice, I. C., & Sykes, M. T. : Representation of vegetation dynamics in the
 778 modelling of terrestrial ecosystems: Comparing two contrasting approaches within European
 779 climate space. *Global Ecology & Biogeography*, 10, 621–637, 2001.

780 Sterling, S. M., Ducharne, A., Polcher, J.: The impact of global land-cover change on the
 781 terrestrial water cycle. *Nat. Clim. Chang.*, 3, 385–390. <http://dx.doi.org/10.1038/nclimate1690>,
 782 2013.

783 Still, C. J., and Berry, J. A.: Global distribution of C3 and C4 vegetation: Carbon cycle
 784 implications, *Global Biogeochem. Cycles*, 17(1), 1006, doi:10.1029/2001GB001807, 2003.

785 Sun, W., Liang, S., Xu, G., Fang, H., and Dickinson, R. E.: Mapping plant functional types from
 786 MODIS data using multisource evidential reasoning, *Remote Sens. Environ.*, 112, 1010–1024,
 787 <https://doi.org/10.1016/j.rse.2007.07.022>, 2008.

788 Swart, N. C., Cole, J. N. S., Kharin, V. V., Lazare, M., Scinocca, J. F., Gillett, N. P., Anstey, J.,
 789 Arora, V., Christian, J. R., Hanna, S., Jiao, Y., Lee, W. G., Majaess, F., Saenko, O. A., Seiler, C.,
 790 Seinen, C., Shao, A., Sigmond, M., Solheim, L., von Salzen, K., Yang, D., and Winter, B.: The
 791 Canadian Earth System Model version 5 (CanESM5.0.3), *Geosci. Model Dev.*, 12, 4823–4873,
 792 <https://doi.org/10.5194/gmd-12-4823-2019>, 2019.

793 Tsendbazar, N. E., de Bruin, S., Mora, B., Schouten, L., Herold, M.: Comparative assessment of
 794 thematic accuracy of GLC maps for specific applications using existing reference data, *Int. J.*
 795 *Appl. Earth Obs. Geoinf.*, 44, 124–135, <https://doi.org/10.1016/j.jag.2015.08.009>, 2016.

796 Wulder, M.A., Nelson, T.: EOSD land cover classification legend report: Version 2, Natural
 797 Resources Canada, Canadian Forest Service, Pacific Forestry Centre, Victoria, British Columbia,
 798 Cana-da, 13 January 2003, 83pp., Available from
 799 http://www.pfc.forestry.ca/eosd/cover/EOSD_Legend_Report-v2.pdf.

800 Wulder, M.A., Bater, C.W., Coops, N.C., Hilker, T., and White, J.C.: The role of LiDAR in
 801 sustainable forest management, *The Forestry Chronicle*, 84 (6), 807- 826, 2008.

802 Wulder, M.A., White, J.C., Bater, C.W., Coops, N.C., Hopkinson, C., Chen, G.: Lidar plots - a
 803 new large-area data collection option: context, concepts, and case study. *Can. J. Remote. Sens.*
 804 38, 600–618, <https://doi.org/10.5589/m12-049>, 2012.

805 Verseghe, D. L.: CLASS—A Canadian Land Surface Scheme for GCMs, I. Soil model, *Int. J.*
 806 *Climatol.*, 11, 111–133, <https://doi.org/10.1002/joc.3370110202>, 1991.

807 Verseghe, D., McFarlane, N., and Lazare, M.: Class - A Canadian land surface scheme for
 808 GCMs. II: Vegetation model and coupled runs, *Int. J. Climatol.*, 13, 347–370,
 809 <https://doi:10.1002/joc.3370130402>, 1993.

810 Wang, A., Price, D. T., Arora, V. K.: Estimating changes in global vegetation cover (1850-2100)
 811 for use in climate models, *Global Biogeochem. Cy.*, 20, <https://doi:10.1029/2005GB002514>,
 812 2006.

813 Wang, L., MacKay, M., Brown, R., Bartlett, P., Harvey, R., and Langlois, A.: Application of
814 satellite data for evaluating the cold climate performance of the Canadian Regional Climate
815 model over Québec, Canada, *J. Hydrometeorol.*, 15, 614–630, [https://doi.org/10.1175/JHM-D-](https://doi.org/10.1175/JHM-D-13-086.1)
816 13-086.1, 2014.

817 Wang, L., Cole, J. N.S., Bartlett, P., Verseghy, D., Derksen, C., Brown, R., von Salzen, K.:
818 Investigating the spread in surface albedo for snow-covered forests in CMIP5 models, *J.*
819 *Geophys. Res. Atmos.*, 121, 1104–1119, <https://doi:10.1002/2015JD023824>, 2016.

820 Wang, L., Bartlett, P., Chan, E., and Xiao, M.: Mapping of Plant Functional Type from Satellite-
821 Derived Land Cover Datasets for Climate Models, In *Proceedings of the 2018 IEEE International*
822 *Geoscience and Remote Sensing Symposium*, Valencia, Spain, 22–27, [https://DOI:](https://DOI:10.1109/IGARSS.2018.8518046)
823 10.1109/IGARSS.2018.8518046, 2018.

824 Wang, L., Bartlett, P., Pouliot, D., Chan, E., Lamarche, C., Wulder, M.A., Defourny, P., Brady,
825 M.: Comparison and Assessment of Regional and Global Land Cover Datasets for Use in
826 CLASS over Canada, *Remote Sens.*, 11(19), 2286; <https://doi.org/10.3390/rs11192286>, 2019.

827 Zakharova, L., Meyer, K. M., Seifan, M.: Trait-based modelling in ecology: A review of two
828 decades of research, *Ecological Modelling*, 407,
829 <https://doi.org/10.1016/j.ecolmodel.2019.05.008>, 2019.

830

831

832

833

834

Table 1. Cross-walking table for mapping the 30 m Hybrid land cover map to CLASSIC PFTs in Canada. Nine PFTs in CLASSIC: NLE - Needleleaf Evergreen trees, NLD - Needleleaf Deciduous trees, BLE - Broadleaf Evergreen trees, BCD - Broadleaf Cold Deciduous trees, BDD - Broadleaf Dry Deciduous trees, C3C – C3 Crops, C4C - C4 Crops, C3G – C3 Grasses, and C4C - C4 Grasses.

ID	Map description	1 NLE	2 NLD	3 BLE	4+5 BCD BDD	6+7 C3C C4C	8+9 C3G C4G	Urban	Lake	Bare
2	Sub-polar taiga needleleaf forest	0.20					0.60			0.20
11	Sub-polar or polar shrubland-lichen-moss						0.65			0.35
12	Sub-polar or polar grassland-lichen-moss						0.45			0.55
13	Sub-polar or polar barren-lichen-moss						0.10			0.90
15	Cropland					1.0				
16	Barren lands									1.0
17	Urban							1.0		
20	Water								1.0	
31	Snow_ice									1.0
32	Rock_rubble									1.0
50	Shrubland				0.20		0.60			0.20
80	Wetland				0.05		0.85			0.10
81	Wetland-treed	0.55			0.05		0.35			0.05
100	Herbs						0.80			0.20
210	Coniferous	1.0								
220	Broadleaf				1.0					
230	Mixedwood	0.50			0.50					

Table 2. The sub-pixel fractional tree cover fraction for ESA-CCI (European Space Agency - Climate Change Initiative) land cover classes (with forest cover) based on the Hansen TCF (Tree Cover Fraction) dataset in Canada. Ratios of TCF between the main class and the closed class, and between the open class and the closed class are also included.

ESA-CCI class	ESA-CCI class description	Tree cover Fraction (%)	Ratio of TCF relative to closed class
30	Mosaic cropland (>50%) / natural vegetation (<50%)	13.7	
40	Mosaic natural vegetation (>50%) / cropland (<50%)	45	
60	Tree cover broadleaved deciduous closed to open (>15%)	68.5	0.8
61	Tree cover broadleaved deciduous closed (>40%)	86.7	1
62	Tree cover broadleaved deciduous open (15-40%)	37.4	0.43
70	Tree cover needleleaf evergreen closed to open (>15%)	39.3	0.6
71	Tree cover needleleaf evergreen, closed (>40%)	61.7	1
72	Tree cover needleleaf evergreen open (15-40%)	23.2	0.38
90	Tree cover Mixed	80.9	
100	Mosaic tree and shrub (>50%) / herbaceous cover (<50%)	37.3	
110	Mosaic herbaceous cover (>50%) / tree and shrub (<50%)	19.6	
120	Shrubland	28.1	
150	Sparse vegetation (tree shrub herbaceous cover) (< 15%)	4	
160	Tree cover, flooded fresh/brackish	43	
180	Shrub or herbaceous cover, flooded	26.9	

Table 3. The sub-pixel fractional composition for ESA-CCI classes (columns, homogenous ESA-CCI pixels) based on the Hybrid land cover map (rows) for dominant land cover classes in Canada. The fractions for NLE and BCD are computed based on equation (1).

Hybrid/ ESACCI Class	Hybrid description	30	40	60	70	71	90	100	120	130	140	150	160	180
2	Sub-polar taiga needleleaf forest				0.02			0.01		0.01				
11	Sub-polar/polar shrubland-lichen- moss										0.01	0.05		
12	Sub-polar/polar grassland-lichen- moss				0.04				0.03	0.01	0.24	0.27	0.03	0.04
13	Sub-polar/polar barren-lichen-moss				0.02			0.01	0.02	0.01	0.34	0.09		0.02
15	Cropland	0.92	0.37	0.02						0.1				
16	Barren lands									0.01	0.15	0.17		
50	Shrubland	0.01	0.07	0.06	0.13	0.05	0.04	0.32	0.46	0.09	0.14	0.25	0.06	
80	Wetland		0.03	0.08	0.2	0.05	0.03	0.27	0.2	0.02	0.06	0.09	0.37	0.75
81	Wetland treed		0.01	0.01	0.17	0.07	0.03	0.11	0.12				0.43	0.15
100	Herbs	0.06	0.27	0.08	0.02		0.02	0.06	0.09	0.72	0.01	0.03	0.01	0.01
210	Coniferous		0.01	0.02	0.29	0.72	0.07	0.04	0.03		0.01	0.02	0.06	
220	Broadleaf	0.01	0.13	0.57	0.02	0.01	0.28	0.07	0.01	0.01			0.01	
230	Mixedwood		0.1	0.14	0.09	0.07	0.52	0.12	0.03				0.02	
NLE	Needleleaf evergreen		0.07	0.09	0.44	0.8	0.32	0.19	0.16	0.01	0.02	0.05	0.31	0.08
BCD	Broadleaf cold deciduous	0.01	0.19	0.66	0.09	0.06	0.57	0.18	0.09	0.02	0.02	0.03	0.05	0.03

871 **Table 4.** Cross-walking table for mapping ESA-CCI land cover dataset to CLASSIC PFTs.

ID	ESA-CCI class description	1 NLE	2 NLD	3 BLE	4+5 BCD BDD	6+7 C3C C4C	8+9 C3G C4G	Urban	Lake	Ocean	Bare
10	Cropland, rainfed (CR)					0.80	0.20				
11	CR Herbaceous cover					0.90	0.10				
12	CR Tree or shrub cover				0.60		0.30				0.10
20	Cropland, irrigated or post-flood				0.05	0.85	0.10				
30	Mosaic cropland (>50%) / natural vegetation (tree, shrub, herb)	0.05			0.15	0.60	0.20				
40	Mosaic natural vegetation (tree, shrub, herb) >50% / crop	0.10			0.20	0.40	0.30				
50	Tree cover broadleaved evergreen closed to open			0.95	0.05		0.0				
60	Tree cover broadleaved deciduous closed to open				0.70		0.25				0.05
61	Tree cover broadleaved deciduous closed				0.90		0.10				
62	Tree cover broadleaved deciduous open				0.40		0.40				0.20
70	Tree cover needleleaf evergreen closed to open	0.85			0.05		0.10				
71	Tree cover needleleaf evergreen, closed	0.85			0.05		0.10				
72	Tree cover needleleaf evergreen open	0.35			0.10		0.40				0.15
73	Replace LC70 in Canada	0.45			0.10		0.30				0.15
80	Tree cover needleleaf deciduous closed to open	0.05	0.40		0.10		0.35				0.10
81	Tree cover needleleaf deciduous closed	0.05	0.80		0.05		0.15				
82	Tree cover needleleaf deciduous open	0.05	0.30		0.10		0.45				0.15
90	Tree cover Mixed	0.25	0.05		0.60		0.10				
100	Mosaic tree and shrub (>50%) / herbaceous cover (<50%)	0.15	0.05		0.20		0.45				0.15
110	Mosaic herbaceous cover (>50%) / tree and shrub (<50%)	0.05	0.05		0.10		0.65				0.15
120	Shrubland				0.30		0.45				0.25
121	Shrubland evergreen	0.15		0.15			0.45				0.25
122	Shrubland deciduous				0.30		0.45				0.25

130	Grassland						0.70				0.30
140	Lichens and mosses						0.20				0.80
150	Sparse vegetation (tree shrub herbaceous cover) (< 15%)				0.05		0.35				0.60
151	Sparse tree (<15%)				0.05		0.35				0.60
152	Sparse shrub (<15%)						0.30				0.70
153	Sparse herbaceous cover (<15%)						0.30				0.70
160	Tree cover, flooded fresh/brackish	0.30			0.10		0.45		0.1		0.05
170	Tree cover, flooded saline water	0.30			0.10		0.40			0.1	0.10
180	Shrub or herbaceous cover, flooded	0.10			0.05		0.45		0.15	0.15	0.10
190	Urban areas	0.02 5			0.025		0.15	0.75	0.05		
200	Bare areas										1.0
201	Consolidated bare areas										1.0
202	Unconsolidated bare areas										1.0
210	Water bodies								1.0		
220	Permanent snow and ice										1.0

872

873

874

875

876

877

878

879

880

881

882

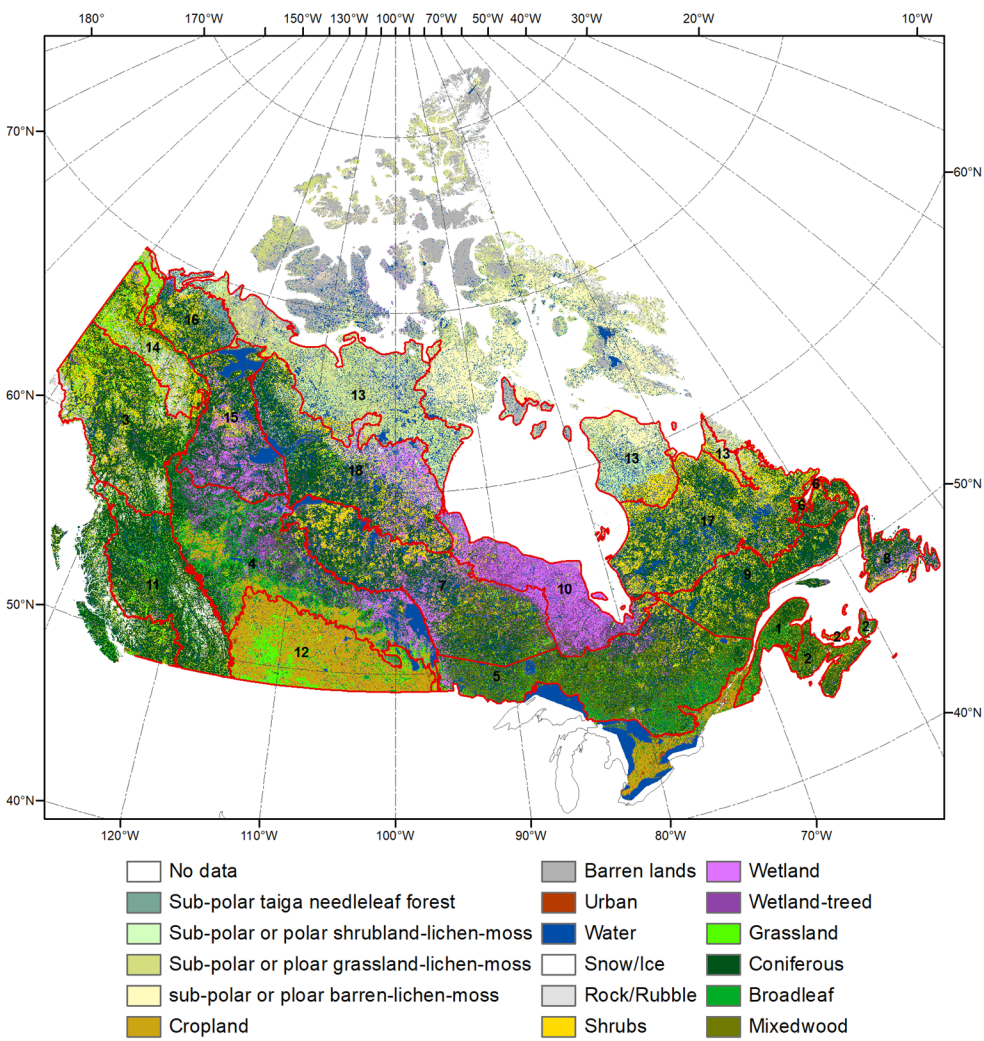
883

884

885

886

887



888

889

Figure 1. The Hybrid land cover map of Canada based on VLCE and NALCMS land cover maps for 2010. The red polygons represent 18 ecozones used in this study.

891

892

893

894

895

896

897

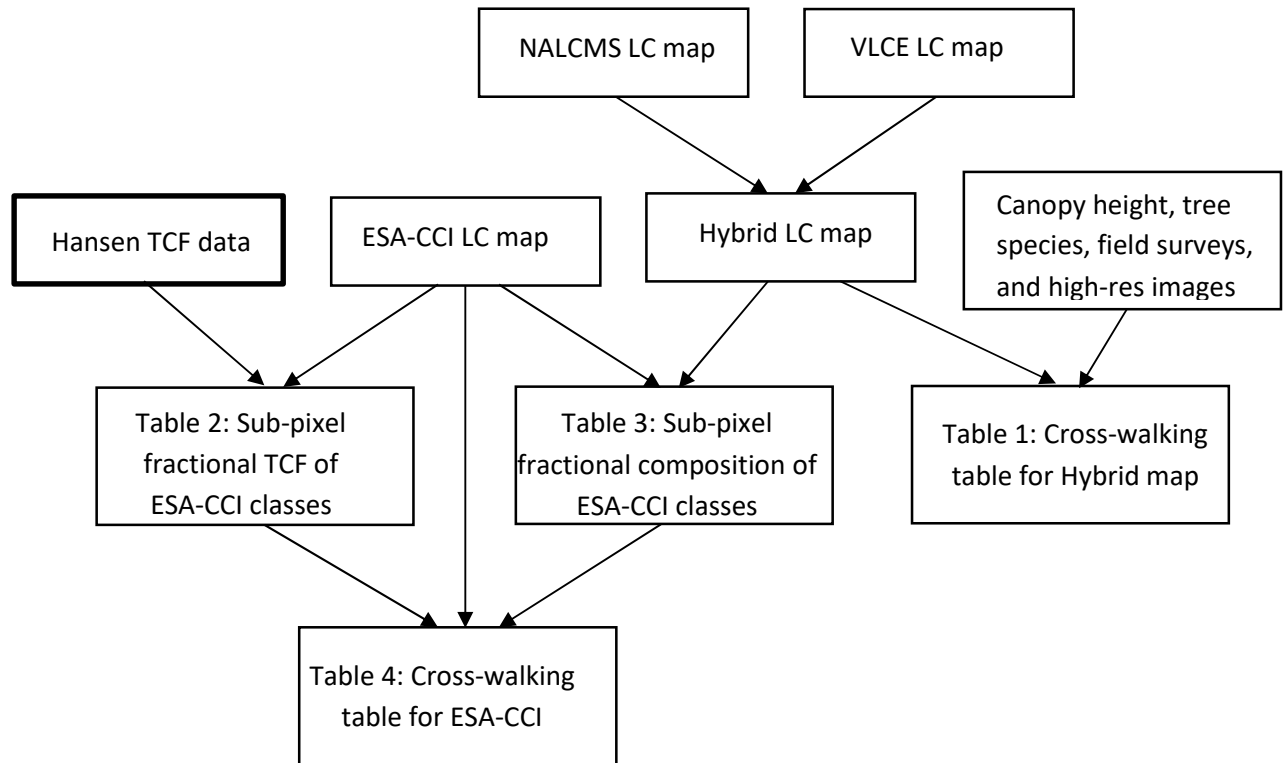
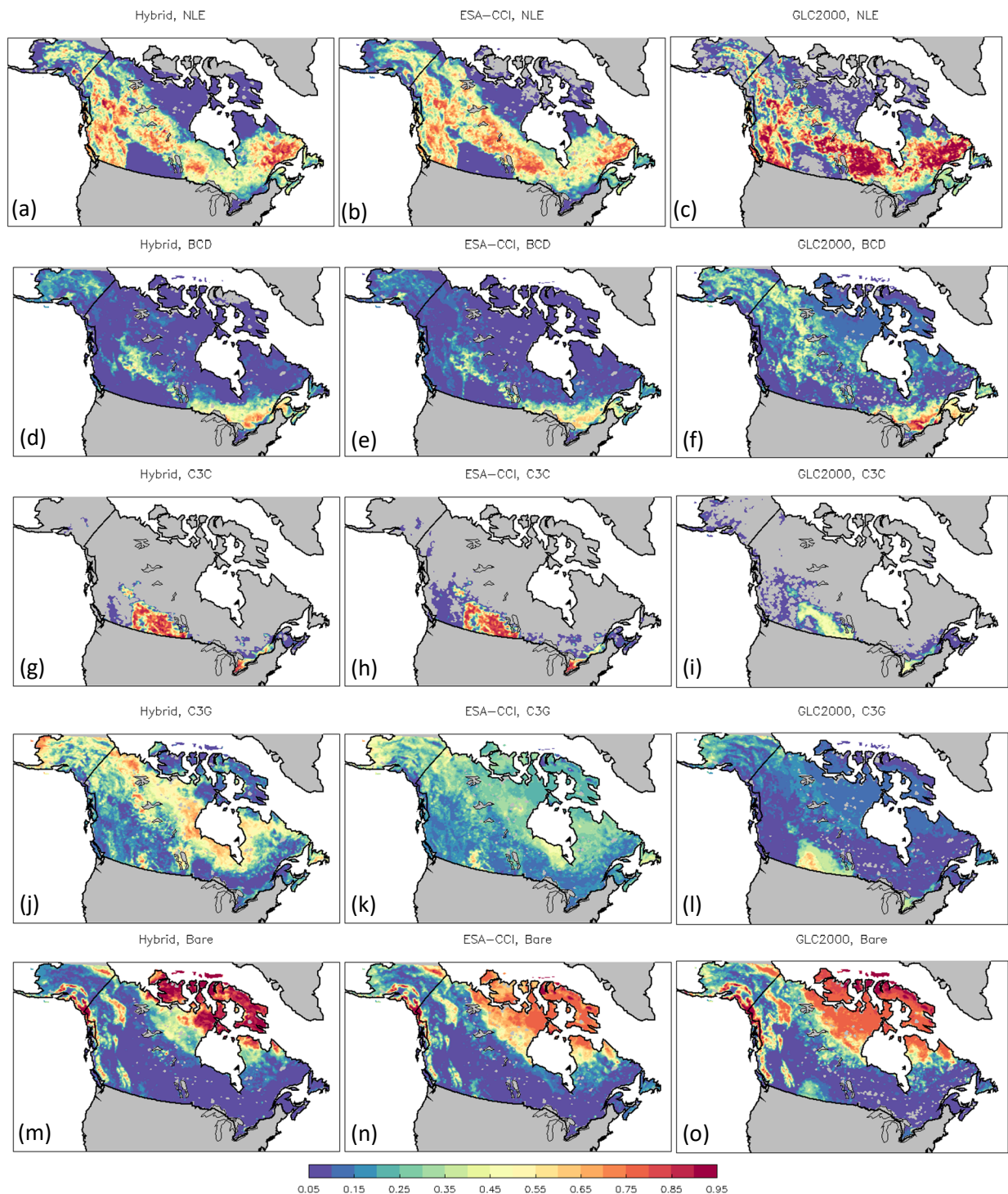


Figure 2. Schematic flow chart of the process for creating the cross-walking table for ESA-CCI land cover (LC) dataset. NALCMS: the North America Land Change Monitoring System; VLCE: the Virtual Land Cover Engine; TCF: Tree Cover Fraction.



913

914 **Figure 3.** The spatial distribution of CLASSIC PFTs based on the Hybrid (left), ESA-CCI (middle), and
 915 GLC2000 (right) land cover datasets respectively. The maps for C4C and C4G are not shown for their
 916 fractions are small (0.5% for C4 crops and 0.1% for C4 grasses) in Canada. The last panel shows fractions
 917 for bare ground from the three datasets.

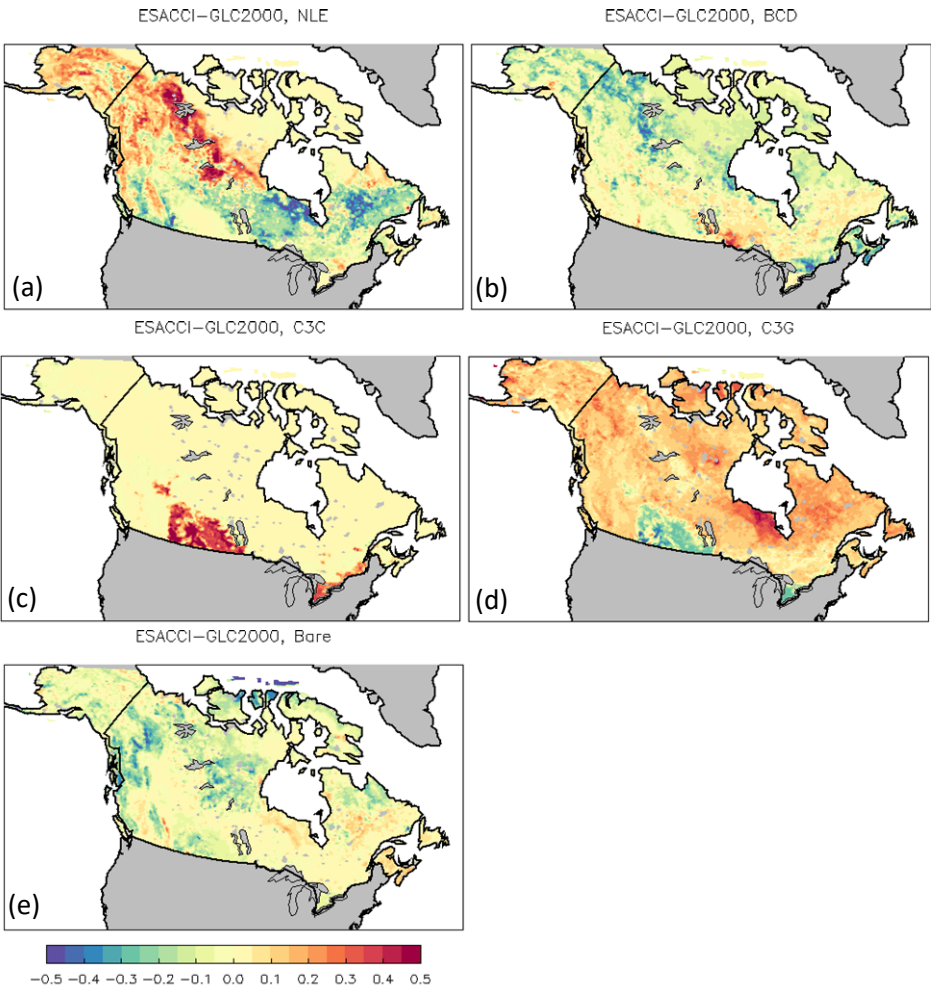
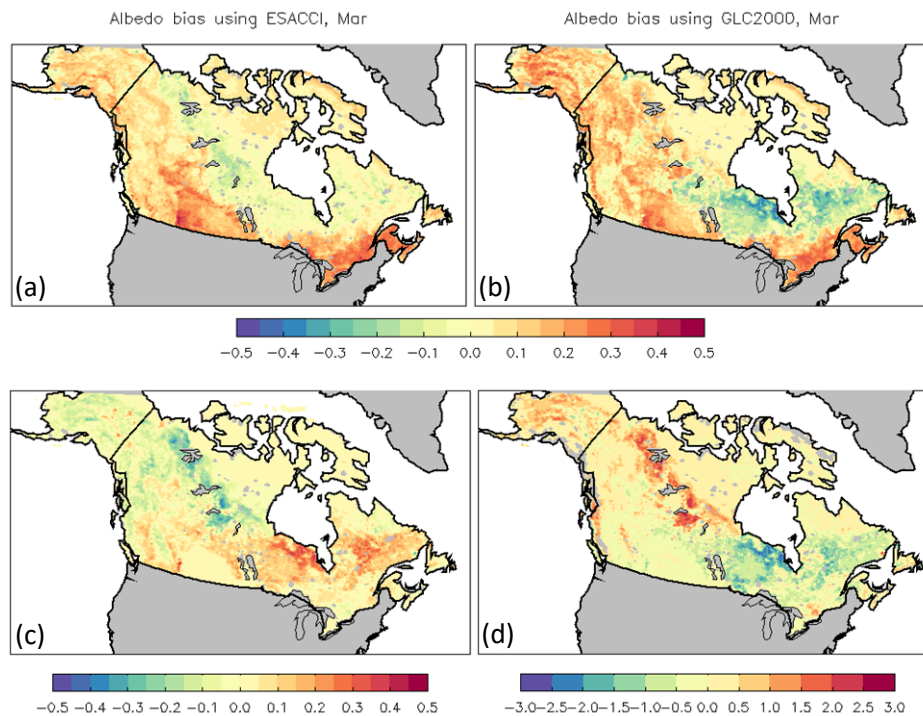


Figure 4. The difference in PFTs based on ESA-CCI and GLC2000 datasets for selected PFTs (a) NLE, (b) BCD, (c) C3C, (d) C3G, and (e) Bare.

945

946



958

959 **Figure 5.** Surface albedo bias (relative to MODIS) in CLASSIC simulations using PFT distributions
 960 based on (a) ESA-CCI, and (b) GLC2000 land cover products. Panels (c) and (d) show the difference in
 961 simulated surface albedo (c) and leaf area index (d) between the two simulations.

962